Received: 10 July 2025 | Revised: 15 October 2025 | Accepted: 23 November 2025

DOI: 10.1002/mp.70195

RESEARCH ARTICLE

MEDICAL PHYSICS

Development of a customizable model for spectral photon-counting detector CT

Mridul Bhattarai[1,2,3] | **Raj Kumar Panta**[2,3] | **W. Paul Segars**[1,2,3] | **Ehsan Abadi**[1,2,3] | **Ehsan Samei**[1,2,3]

[1]Center for Virtual Imaging Trials, Department of Radiology, Duke University, Durham, North Carolina, USA

[2]Center for Virtual Imaging Trials (CVIT), Duke University, Durham, North Carolina, USA

[3]Department of Radiology, Duke University School of Medicine, Durham, North Carolina, USA

Correspondence
Mridul Bhattarai, Center for Virtual Imaging Trials, Department of Radiology, Duke University School of Medicine, Durham, NC 27707, USA.
Email: bhattaraimridul@gmail.com and mridul.bhattarai@duke.edu

Present address
Raj Kumar Panta, Massachusetts General Hospital, Boston, Massachusetts, USA

Funding information
NIH, Grant/Award Numbers: P41EB028744, R01EB001838, R01HL155293

Abstract

Background: Photon-counting detector CT (PCD-CT) is a new CT technology that offers enhanced spatial and spectral imaging performances. As a new technology, conditioning and qualifying its precise performance can benefit from a comprehensive framework to evaluate task-generic and task-specific image qualities.

Purpose: To develop and validate a customizable and physics-informed simulation framework capable of modeling spatio-energetic detector responses for various PCD designs, integrate it into a virtual imaging framework, and demonstrate its applicability in clinically relevant imaging tasks.

Methods: A customizable simulation model, DukeCounter, was developed to replicate real PCD-CT systems. Photon transport and crosstalk in PCDs were modeled using Monte Carlo simulations, and charge sharing was implemented using an analytical Gaussian charge cloud model. The fundamental interactions in PCDs, including photoelectric absorption, Compton and fluorescence x-ray scatterings, charge cloud formation, and charge diffusion and repulsion, were modeled. Spatio-energetic detector responses were generated for face-on CdTe-, CZT-, GaAs-, and edge-on Si-based PCDs. These responses, combined with standardized scanner parameters, were integrated into a CT simulator to create virtual DukeCounter PCD-CT scanners. The framework was benchmarked against experimental data from a clinical CdTe-based PCD-CT scanner across three dose levels. To demonstrate its utility, three pilot studies were conducted using a computational ACR phantom for task-generic image quality assessment, an XCAT model with bronchitis and emphysema for COPD biomarker extraction, and an XCAT with liver lesions for lesion detectability analysis.

Results: The simulated charge cloud size increased with energy and was more pronounced in Si due to its low atomic number. The detector response across a 3×3-pixel neighborhood varied with PCD material, design, and energy threshold settings. Validation results demonstrated strong agreement between simulated and real ACR images. For the 20-keV-threshold images, the mean relative difference (MRD) in f_{50} of MTF was 4.15% ± 1.21 for air and 2.54% ± 2.08 for bone, and the MRD in f_{av} of NPS was 0.83% ± 0.97. The MRDs in noise magnitude were 2.65% ± 1.68, 3.05% ± 1.97, and 2.78% ± 1.79 for the 20-keV-threshold, 65-keV-threshold, and 70-keV-VMI images, respectively. The MRDs in CT number for the same image types were 0.03% ± 0.03, 0.11% ± 0.09, 0.11% ± 0.05 for air, and 1.85% ± 0.20, 1.84% ± 0.55, 0.50% ± 0.36 for polyethylene. DukeCounter-generated images showed that task-generic and task-specific image qualities were influenced by PCD materials, designs, and energy threshold settings. GaAs-based DukeCounter exhibited the highest

image noise, the largest error in COPD biomarker quantification, and the lowest performance in liver lesion detection, under consistent acquisition and reconstruction settings.

Conclusions: A customizable, modular simulation framework was developed to model spatio-energetic detector responses for various PCD materials and designs. The detector responses were integrated into a CT simulation pipeline to build DukeCounter PCD-CT systems. The framework's utility was demonstrated through task-specific assessments of image quality and clinical performance of DukeCounter systems using XCAT phantoms. This approach enables systematic PCD-CT design evaluation and optimization, supporting translational research in medical imaging by reducing the cost, time, and radiation burden of physical experiments.

KEYWORDS
CT simulation, photon counting detector CT, spatio-energetic detector response

1 | INTRODUCTION

Photon-counting detector computed tomography (PCD-CT) is an expanding spectral CT technology that utilizes semiconductor-based photon-counting detectors (PCDs). PCDs measure the energy of individual photons and assign them to different energy bins. This feature enhances PCD-CT image quality by eliminating electronic noise, offering higher image contrast, and enabling multi-energy material decomposition capabilities.[1,2] Despite these advantages, PCDs are subject to signal degradation processes such as crosstalk and pulse pileup. Crosstalk occurs due to the emission and reabsorption of x-ray photons between detector pixels, attributed to Compton- and x-ray fluorescence-scatterings, along with charge sharing induced by the spread of charge cloud across multiple detector pixels. Pulse pileup occurs due to the limited readout speed of the electronics, leading to accumulation of simultaneous pulses.[2] These non-idealities in PCDs affect overall PCD-CT image quality; however, the existence of clinically-approved and experimental prototype scanners suggests that their deteriorating effects can be mitigated.[3]

As new PCD-CT systems seek clinical approvals and as vendors work on building new prototypes, it is important to develop a framework that can comprehend and characterize the performance of PCD-CT systems based on both task-generic and task-specific image qualities. Such studies with physical scanners and phantoms are costly and time-consuming. While physical phantoms with anthropomorphic features do exist, they are often limited in numbers and cannot fully capture the anatomical variability and population heterogeneity needed for comprehensive task-specific image quality characterization. Another approach is to utilize human subjects; however, such studies are not only costly, time-inefficient, and ground-truth limited, but also involve experimental radiation exposure and further are not possible for new prototypes. Furthermore, the physical characteristics of PCDs and the geometrical specifications of PCD-CT scanners are often safeguarded as proprietary information, making it challenging to systematically study PCD-CT image quality. A viable approach to address these challenges is to utilize a virtual or *in-silico* imaging framework using realistic and customizable models to simulate the physics of signal generation in PCDs and the physics of imaging acquisition across a diverse set of computational human models.[4]

Prior studies have modeled signal detection processes across various PCD materials and designs using cascaded parallel, analytical, and Monte Carlo approaches.[5–12] Despite providing valuable insights, these studies do not provide a generalizable model for simulating diverse PCD designs and materials and often have limited validations against physical measurements. One study presents a framework for modeling charge sharing and pulse pileup in CdTe-based PCDs; however, it lacks validation of the CT image generation pipeline and does not account for initial charge cloud size.[13] Other studies have successfully presented validated simulations of clinical and experimental PCD-CT prototypes but have not explored image quality across PCD-CT scanners.[14,15] As informative as these studies are, there remains a gap in developing a customizable platform that integrates realistic modeling of various PCD designs with an efficient CT image generation framework, comprehensively validated against a clinical PCD-CT scanner.

Our previous work on *in-silico* simulations focused on developing and advancing CT simulator and digital phantoms but lacked a validated tool for generating spatio-energetic detector responses for different PCDs.[14,16–20] The purpose of this study was to develop a customizable detector model that parameterized the signal-generation process for diverse PCD materials and designs and integrate it into an *in-silico* imaging

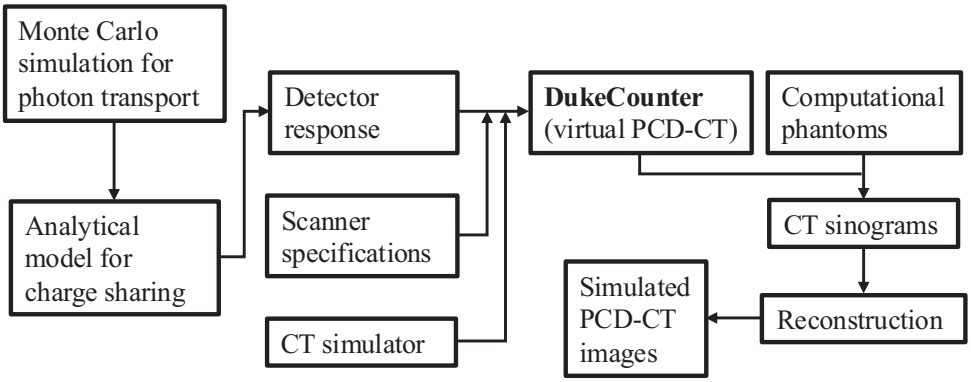

FIGURE 1 A simulation framework of DukeCounter.

framework to enable systematic modeling and characterization of PCD-CT under various detector specifications and energy settings. This framework enables evaluation and optimization of PCD-CT technologies not only in developmental and pre-clinical stages but also in the clinical stage by defining protocols expected to offer task-specific clinical value.

2 | METHODS

The framework of this study is illustrated in Figure 1 and further explained in the subsections below. In summary, the framework involved utilizing Monte Carlo to simulate the quantum detection efficiency of a PCD by modeling photon transport and crosstalk due to Compton and fluorescence scatterings, further blurring it with charge sharing, defining standard CT components, and integrating them into an imaging framework acquainted with a CT simulator, computational phantom or human models, and an image reconstruction tool.

2.1 | Detector response

In this study, detector response refers to the spatio-energetic point spread function, representing the distribution of photon counts across the central and neighboring pixels when a photon of a given energy is incident on the central pixel. Detector response was characterized for all energy threshold settings, where a photon with energy E was registered in energy threshold T_i if an energy $E \geq T_i$ was absorbed in the detector. It included both spatio-energetic mean and covariance matrices across all combinations of detector pixels and energy thresholds. We utilized Monte Carlo simulation to model the stochastic interaction of x-ray photons with the detector and added an analytical Gaussian charge cloud-based model to incorporate charge sharing effect.[21,22]

2.1.1 | Monte Carlo modeling of photon transport

A Monte Carlo (MC) simulation was built in Geant4 (v10.6), a C++ based toolkit, with Livermore physics list. The Livermore physics list modeled the relevant interactions (photoelectric absorption, Compton and Rayleigh scattering, fluorescence, Bremsstrahlung, ionization) between x-ray photons and the semiconductor-based detector material in the diagnostic energy range. Photon step-length cutoffs were set at 0.01 mm in the detector bulk (or wafer) and 0.001 mm in the inter-wafer high-Z foil.

The simulation featured a large 100 × 100-pixel array along the *x*-*y* plane to avoid the boundary effects. A point monoenergetic source with energies ranging from 1 to 120 keV was used to irradiate 10^4 photons perpendicularly onto each location of a 10 × 10 grid of equally spaced points within the central detector pixel for both face-on and edge-on detector designs (Figure 2). This approach ensured a uniform mapping of photon hits across the entire central pixel. The (x, y, z) coordinates and energy of interactions that resulted in energy deposition were logged.

2.1.2 | Charge sharing simulation

An analytical charge sharing model was developed in MATLAB (v R2024a). We formed a 2D Gaussian charge cloud at each interaction location derived from the MC simulation. We assumed the energy shared between pixels due to charge sharing to be proportional to the area of the charge cloud projected on those pixels.[9] The electric field direction was along the z-axis for the face-on detector design and along the y-axis for the edge-on design. Because of the high-Z inter-wafer barrier (Figure 2), charge sharing could only occur in the *x*-direction for the edge-on PCD design, while it could occur in both *x*- and *y*-directions for the face-on PCD

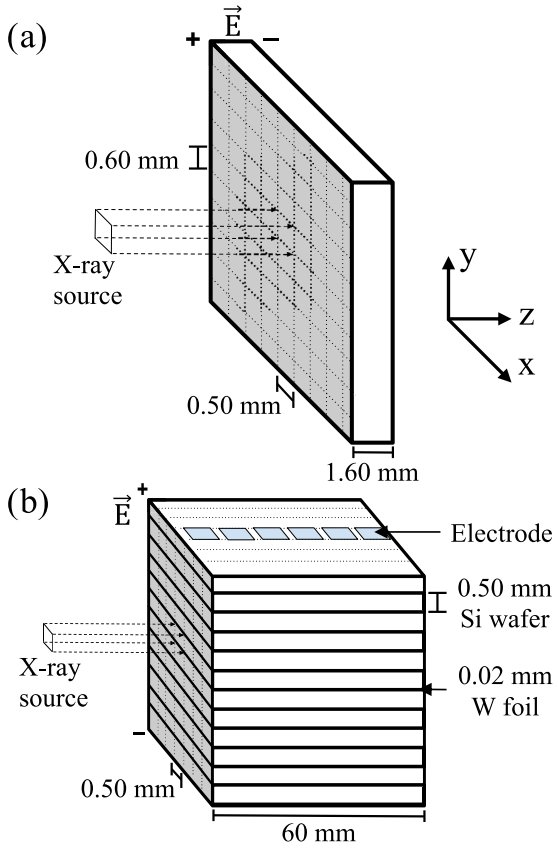

FIGURE 2 Example of the (a) face-on (CdTe, CZT, and GaAs) and (b) edge-on (Si with W) simulation geometries. X-ray photons impinge in the direction (0, 0, −1).

design. The lateral spread of charge cloud across detector pixels was modeled with the standard deviation σ (**Equation 1**), which was derived at the 2D x–y plane by collapsing 3D drift, diffusion, and repulsion process. For each detector pixel, the shared fraction of energy due to charge sharing was computed by integrating the charge density computed using σ with the pixel boundaries as the limits of integration. If $\sigma << $ pixel pitch, the probability of charge sharing beyond the neighboring pixels would be negligible, limiting charge sharing across a maximum of two pixels (along x-direction) for edge-on and four pixels (along x and y directions) for face-on PCDs.

The standard deviation (σ) of the 2D Gaussian charge cloud was defined as

$$\sigma = \sqrt{2\frac{k_B T z d}{qU} + \left(\frac{zdNq}{10\pi\varepsilon U}\right)\frac{1}{\sqrt{5}\sigma_i} + {\sigma_i}^2} \qquad (1)$$

where k_B = Boltzmann's constant, T = absolute temperature, z = distance between interaction point and the anode along the direction of electric field, d = detector thickness along the direction of electric field, q = elementary charge, U = bias voltage, N = number of electron-hole pairs liberated in each interaction (=E_{dep}/Δ_E), where E_{dep} is energy deposited in each interaction and Δ_E is the energy required to liberate one electron-hole pair), ε = permittivity (= $\varepsilon_R \times \varepsilon_0$, where ε_R is the relative permittivity of the semiconductor material and ε_0 is the vacuum permittivity), and σ_i = initial radius of the charge cloud.[23] We also modeled the fluctuations in e-h pairs generation (computing N) using the Fano factor. In this way, the σ provides a spatial distribution of the charges inside the charge cloud, accounting for charge diffusion and charge repulsion along the parallel and perpendicular directions of the electric field, respectively. The values for the constants used in computing for different PCD materials are tabulated in Table 1.

The bias voltage (U) determines the electric field strength, defined as the ratio of the applied bias voltage to the detector thickness along the field direction. Electric field affects the drift velocity and mobility of charge carriers, particularly electrons moving toward the anode. In this study, bias voltages were not optimized, but were chosen based on prior work to achieve a field strength of approximately 6000–7000 V/cm.[24,25] The bias voltages are chosen to balance between charge collection efficiency and breakdown or polarization risk, though a comprehensive optimization was beyond the scope of this study.

We designed a separate MC simulation in Geant4 to compute the initial radius of the charge cloud (σ_i). A point electron source was placed at the center of a cubicle semiconductor-material block to irradiate 10^5 electrons at each energy (1 keV to 120 keV) in all directions. The radius covering 95% of the total charge was considered as the initial charge cloud radius, following the approach used in prior work.[10] In this way, charge sharing was modeled by creating a charge cloud at each interaction point and simulating initial charge cloud size, charge repulsion, and charge diffusion.

2.1.3 | Detector materials and geometries

The detector modeling approach was applied to four pivotal PCD materials – Cadmium Telluride (CdTe; Z = 48/52), Cadmium Zinc Telluride (CZT; Z = 48/30/52), Silicon (Si; Z = 14), and Gallium Arsenide (GaAs; Z = 31/33) using face-on and edge-on designs. For the CdTe-, CZT-, and GaAs-PCDs, we used a face-on design with a continuous array of pixels measuring 0.50 mm × 0.60 mm and a thickness of 1.60 mm (Figure 2a). For the Si-PCD, considering Silicon's low-Z characteristics, which entail lower absorption efficiency and higher Compton scattering than high-Z materials, we used an edge-on design and inserted a 0.02-mm Tungsten (W; Z = 74) foil between consecutive Silicon wafers, leading to an array of pixels measuring 0.50 mm × (0.50 + 0.02) mm and a thickness of 60 mm (Figure 2b). The inclusion of W in the Si-PCD design prevents the scattering of

TABLE 1 Constants for various PCD materials used to compute σ.

	CdTe	CZT	GaAs	Si
k_B	1.38×10^{-23} J/K			
T	313.15 K			
Q	1.60×10^{-19} C			
U	1000 V			375 V
Δ_E	4.4 eV	4.6 eV	4.2 eV	3.6 eV
Fano factor	0.12	0.14	0.12	0.11
ε_0	8.85×10^{-12} CV^{-1} m^{-1}			
ε_R	10.2	10	13.1	11.7

TABLE 2 DukeCounter CT scanner components.

Anode angle	8
Focal spot	1.0 mm × 1.0 mm
Number of channels (fan angle)	1640
Number of rows (cone angle)	128
Detector pixel size (fan angle × cone angle)	0.50 mm × 0.60 mm (CdTe, CZT, GaAs) 0.50 mm × 0.50 + 0.02 mm (Si + W)
Source-to-isocenter distance	575 mm
Source-to-detector distance	1104 mm (CdTe, CZT, GaAs) 957 mm (Si)
Projections per rotation	2000

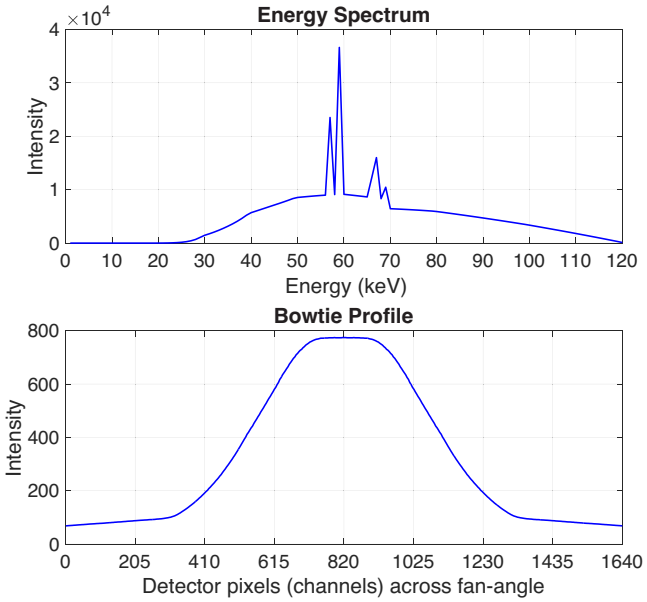

FIGURE 3 Energy spectrum (top) summed across all channels and bowtie profile (bottom) summed across all energies from 1 to 120 keV.

x-ray photons across detector pixels in one dimension, decreasing the probability of multiple counts from one incident photon at the cost of the quantum efficiency of the detector.[9,26]

The PCD geometries (Figure 2) depicted in this study were implemented to cover a range of geometries commonly proposed and utilized in various clinical PCDs.[8,26–30] Our objective, however, was not to replicate any specific PCD design but showcase the generic nature of our simulation framework. Our framework can accommodate other PCD configurations, such as an edge-on GaAs-based PCD utilizing a GaAs wafer coupled with a chromium (Cr) foil.[31,32] Utilizing MC simulation and charge sharing model, we generated detector responses for face-on CdTe-, CZT-, GaAs-, and edge-on Si-based PCDs (Figure 2).

2.2 | DukeCounter scanner components

A set of standardized CT scanner components (Table 2) were defined to design virtual scanner models of CdTe, CZT, GaAs, and Si PCD-CT, which we collectively call the DukeCounter scanners. This allowed us to keep a uniform set of scanner components for all PCD simulations.

A 120 kV poly-energetic spectrum (Figure 3, top) from a Tungsten anode target post 4-mm Aluminum filter was estimated using an established toolkit.[33] Similarly, an intensity profile across the fan angle (Figure 3, bottom) was derived for a 40.75-degree fan angle and an aluminum-based beam-shaping bowtie filter using a publicly available dataset, which reported the thickness of aluminum across fan angle for a "medium" bowtie design, representing a typical clinical configuration.[34] The modeled bowtie filter can introduce beam-hardening effects in the resulting projection images. DukeCounter CT detector pixels were assembled into a cylindrical array without any dead space. The beam collimation was set to 40 mm at the isocenter for all DukeCounter scanners. An anti-scatter grid was added to achieve a typical scatter-to-primary ratio of 0.08 to 0.10 for a 20-cm water phantom.[35]

2.3 | CT simulator

To efficiently generate realistic and scanner-specific PCD-CT sinograms, a validated CT simulator (DukeSim) was utilized.[14,16] DukeSim calculates primary and scatter signals using ray-tracing and Monte Carlo, respectively. In this study, the detector responses for all PCD designs and the scanner components of DukeCounter CT were incorporated into DukeSim. The proposed framework can model spatio-energetic detector response across user-defined spatial extents (e.g., 3 × 3, 5 × 5, 7 × 7) and varying numbers of energy thresholds. To integrate with the current configuration of the DukeSim simulator, detector responses were extracted for 3 × 3-pixel arrays around the center pixel and for two energy thresholds LT and HT (LT < HT) for all PCDs, where LT and HT stand for low-threshold and high-threshold, respectively. For CdTe-, CZT-, and GaAs-based PCDs, LT and HT were set to 20 keV and 65 keV, respectively, while for the Si-PCD they were set to 5 keV and 35 keV. The 3 × 3-pixel binning of detector response has proved effective to adequately represent the signal crosstalk for PCDs made from high-Z materials.[12] In contrast, for Si-based PCDs, the use of high-Z W foils reduces some crosstalk along the *y*-axis; however, due to Si low-Z characteristics, crosstalk can still extend beyond a 3 × 3-pixel array. To evaluate the impact of simulating 3 × 3-pixel array for Si-based PCD, the spectral response and source-spectrum-weighted modulation transfer function (MTF) were measured for 3 × 3 and 5 × 5-pixel arrays, following methods described in previous studies.[12,36] Using a 3 × 3-pixel array instead of a 5 × 5 resulted in 5.9% and 3.1% signal loss at the 5 keV and 35 keV thresholds, respectively. Similarly, the 3 × 3 MTF was greater than 5 × 5 MTF by 5.9% ± 2.0 and 2.9% ± 1.0 for the same thresholds, indicating that the 5 × 5 array captured increased spatial blurring in Si-based PCD (Figure 4). These findings suggest that extending the simulated array to a 5 × 5 configuration could reduce signal loss in Si-PCD simulations; however, since the CT simulator is limited to processing up to a 3 × 3-pixel array, detector responses for the Si-based PCD were also generated for a 3 × 3 configuration. Nonetheless, importantly, the proposed framework is flexible and can compute detector responses for pixel arrays of arbitrary size.

DukeSim calculates the noise-free mean signal for each detector element *p* across *n* energy thresholds, ET_k ($k = 1, 2, 3, \ldots, n$) as

$$S(p)_{1\times n} = \sum_{E}\sum_{i,j=1}^{i,j=3} N(E)_{i,j} \times R(E,\ ET_k)_{i,j},\ k = 1,\ 2,\ 3,\ \ldots,\ n \tag{2}$$

where *(i, j)* is the pixel index within the 3×3 array with center at (2, 2), $N(E) \in R^{3\times3}$ is the number of photons at energy *E* incident on the 3×3 pixel array around the center pixel *p* after attenuating through the phantom, $R(E, ET_k) \in R^{3\times3}$ is the detector response, that is, the probability of a photon with energy *E* being recorded in the 3×3 pixel array at an energy threshold ET_k. The correlated noisy signal for *n* energy thresholds is then calculated using multivariate Gaussian random variables with mean $S(p)_{1\times n}$ and covariance matrix $C(p)_{n\times n}$ computed as

$$C(p)_{n\times n} = \begin{bmatrix} Cov(p, ET_1, ET_1) & \ldots & Cov(p, ET_1, ET_n) \\ \ldots & \ldots & \ldots \\ Cov(p, ET_n, ET_1) & \ldots & Cov(p, ET_n, ET_n) \end{bmatrix} \text{and}$$

$$Cov(p, ET_x, ET_y) = \sum_{E}\sum_{i,j=1}^{i,j=3} N(E)_{i,j} \times Cov(E, ET_x, ET_y)_{i,j},$$

$$x, y = 1, 2, \ldots, n, \tag{3}$$

where $Cov(E, ET_x, ET_y) \in R^{3\times3}$ is the spatio-energetic covariance matrix.[14]

To generate realistic noisy sinogram data, the transmitted photon counts for each detector pixel were first multiplied by the mean spatio-energetic detector response (Eq. 2) to obtain the expected noise-free signal across *n* energy thresholds. Then, correlated noise was introduced by sampling from a multivariate Gaussian distribution whose covariance matrix (Eq. 3) captured both the spatial correlations among neighboring pixels and spectral correlations among energy thresholds. This approach ensured that the simulated data preserved realistic mean signal behavior and noise correlations across spatial and spectral domains. The noisy sinogram data were then logged with air normalization and corrected for beam hardening using a polynomial fit derived from polyenergetic and monoenergetic water phantom images across various thicknesses.[16] Scatter from the object in the field of view was not corrected but minimized using an anti-scatter grid as described in Section B (Methods).

The integration of spatio-energetic detector responses and CT scanner components into DukeSim enable the simulation of virtual CdTe-, CZT-, GaAs-, and Si-DukeCounter PCD-CT scanners and efficient formation of PCD-CT sinograms from computational phantoms.

2.4 | Clinical validation

For validation purposes, DukeCounter was adapted to model the scanner geometry of a clinical CdTe-based PCD-CT (NAEOTOM Alpha, Siemens Healthineers). A scanner-specific detector response was generated for a 0.30-mm square pixel and integrated into DukeSim. An ACR CT accreditation phantom was scanned and

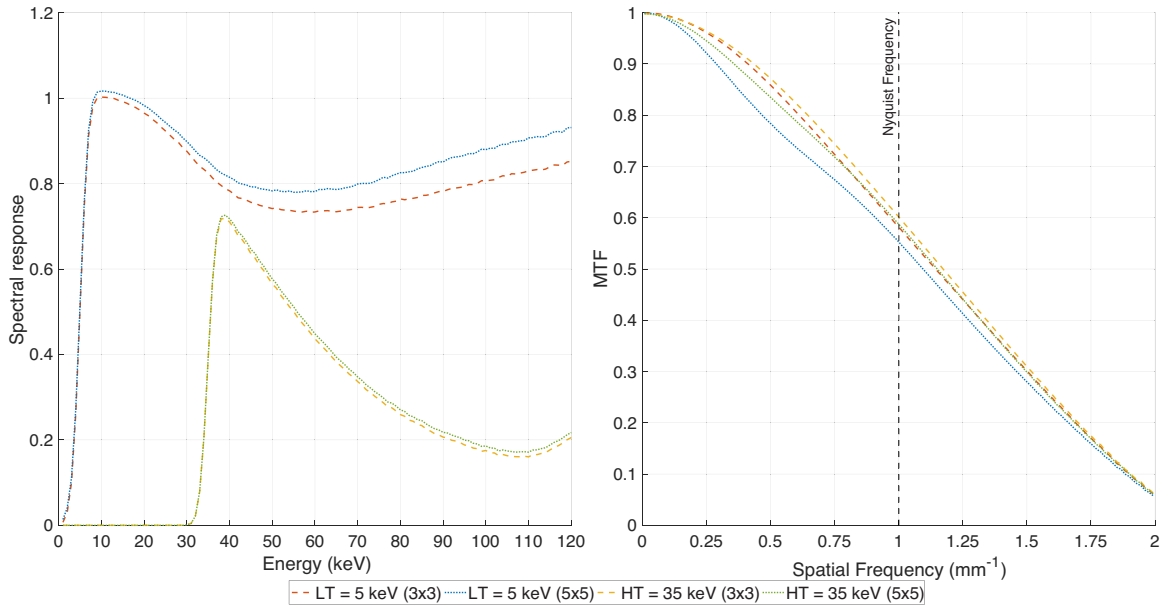

FIGURE 4 Spectral response (left) and source-spectrum-weighted MTF (right) for the simulated Si-based PCD, shown for a 3 × 3 and 5 × 5-pixel arrays at two thresholds – 5 and 35 keV. The spectral response was obtained by summing the mean detector response over the desired spatial extent (3 × 3 or 5 × 5), while the MTF was computed based on methods presented in prior studies.[12,36]

simulated under the same settings at three dose levels of 3.0, 6.0, and 12.0 mGy acquired with a tube voltage of 120 kV, a beam collimation of 144 × 0.4 mm, a gantry rotation speed of 0.50 s per rotation, and a pitch of 1.0. Both the acquired real and simulated sinograms were reconstructed using a vendor-specific reconstruction software (ReconCT version 15.055067.0, Siemens Healthineers) with the same settings – Quantum Iterative Reconstruction (QIR) algorithm of iterative strength 3, Br40 kernel, 250 mm FOV, 512×512 matrix size, and a 0.4 mm slice thickness – to acquire 20-keV and 65-keV threshold images and 70-keV virtual monoenergetic images (VMI). However, clinical CT systems often incorporate proprietary post-processing such as scatter and beam-hardening corrections, which may introduce differences between the simulated and real CT images.

The modulation transfer function (MTF) for air and bone inserts, and the normalized noise power spectrum (nNPS) were measured from 20-keV-threshold real and simulated CT images. As noise magnitude and CT number of air and polyethylene inserts are varied across 20-keV- and 65-keV-threshold images and 70-keV-VMI images, noise magnitude and CT number were measured for all image types from both real and simulated CT images. The spatial frequencies at which the MTF dropped to 90%, 50%, 10% were recorded as f_{90}, f_{50}, f_{10}, respectively. Similarly, the average frequency of the NPS was recorded as f_{av}. These scalar metrics were used to compare spatial resolution and noise texture between the real and simulated CT images.

2.5 | Pilot virtual imaging demonstrations

The utility of the proposed methodology was demonstrated by characterizing DukeCounter scanners for both task-generic and task-specific scenarios. For the task-generic study, a computational model of an ACR CT accreditation phantom was simulated with two tube currents to simulate low- and routine-dose conditions. One task-specific study was focused on quantifying chronic bronchitis and emphysema in chronic obstructive pulmonary disease (COPD) patients by utilizing an anthropomorphic, computational, voxelized human model with emphysema and bronchitis (COPD-XCAT).[37–39] Another study was focused on assessing liver lesion detectability. Six hypoattenuating small liver lesions of different sizes (0.4 cm to 1.5 cm) were inserted in random locations within liver parenchyma of an XCAT. These lesions were iodinated, simulating the portal venous phase in a contrast-enhanced imaging study.[40]

The computational ACR and two human models were imaged using the CdTe-, CZT-, GaAs-, and Si-based DukeCounter scanners with the acquisition settings tabulated in **Table 3** to generate two energy threshold images – low-threshold (LT) and high-threshold (HT). LT and HT were 20 and 65 keV for CdTe-, CZT-, and GaAs-DukeCounter scanners, whereas 5 and 35 keV was used for Si-DukeCounter, per operating expectations of corresponding scanners. The resulting sinograms were reconstructed using an open-source multi-channel reconstruction (MCR) toolkit with reconstruction settings

TABLE 3 Image acquisition and reconstruction settings for the computational ACR phantom, COPD-XCAT, and XCAT with liver lesions.

		ACR	COPD-XCAT	Liver lesion-XCAT
Acquisition settings	Tube voltage	120 kV		
	Tube current	40 mA and 200 mA	320 mA	240 mA
	Pitch	0.8		
	Gantry rotation speed	0.5 s		
Reconstruction settings	Image type	LT and HT	LT	70 keV – mono-energetic
	Recon algorithm	Weighted-filtered back projection (wFBP)		
	Recon kernel	Hann (smooth)	Ram-Lak (sharp)	Hann (smooth)
	Slice thickness	1 mm	1 mm	3 mm
	Pixel size	0.41×0.41 mm^2	0.41×0.41 mm^2	0.44×0.44 mm^2

tabulated in Table 3.[41] Furthermore, 70-keV monoenergetic images for all PCD-CT systems were generated using a standard two-material decomposition.[42] Cylindrical phantoms containing known iodine and calcium concentrations were scanned at high dose with each modeled DukeCounter system and corresponding two energy thresholds to obtain calibration data, which were then applied to reconstruct 70-keV monoenergetic CT images.

From the ACR phantom images, the MTF for the air insert, noise magnitude, and CT number of the bone insert were measured from the LT and HT images. From the COPD-XCAT images, Pi10 – a clinically significant biomarker for bronchitis – was measured from the ground-truth and LT images and the absolute differences between these measurements were reported. Pi10 represents the square root of the wall area around an airway with a 10 mm perimeter.[38,39] In addition, mean absolute error (MAE) was calculated to assess the accuracy of density measurements for emphysema, defined as the voxel-wise mean absolute difference between the ground-truth and LT images. The ground-truth consisted of cross-sectional images of the COPD-XCAT phantom at 66 keV, the effective energy of the source spectrum. For the XCAT with liver lesions, 70-keV mono-energetic images were derived from the LT and HT images to compute CNR for each lesion with liver as the background. Additionally, a detectability index was measured for each of those lesions to assess the likelihood of its detectability by a human reader.[40,43]

Task-independent detective quantum efficiencies (DQEs) were computed for a 0.30 × 0.30 × 1.60 mm^3 CdTe-PCD (configuration simulated for clinical validation) using 20 and 65 keV thresholds, and for a 0.50 × 0.50 × 60 mm^3 Si-PCD using 5 and 35 keV thresholds, following the methodology defined in prior studies.[12,36,44] Transmitted spectra after attenuation through water phantoms of various thicknesses (20, 30, 40 cm) were used to measure the DQEs, consistent with the approach adopted in those studies.

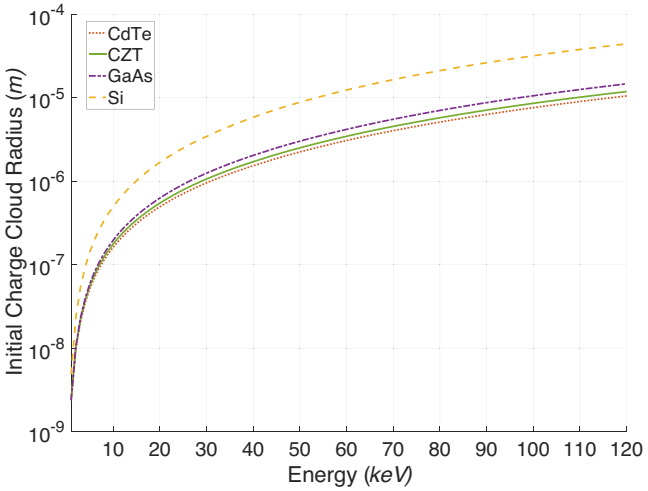

FIGURE 5 Initial charge cloud radii for different PCD materials. It was defined as the radius covering 95% of the total charge generated by 10^5 electrons with energies ranging from 1 to 120 keV. The *y*-axis is shown on a logarithmic scale.

This comparison corroborates the methodological consistency and validity of our framework relative to prior simulation-based studies.

3 | RESULTS

3.1 | Detector response

Figure 5 shows the radius of the spherical charge cloud for each PCD material calculated using MC simulation. The size of the initial charge cloud increased more rapidly for Si (0.005–44.336 um) than for GaAs (0.002–14.706 um), CdTe (0.002–10.522 um), or CZT (0.003 um to 11.876 um) as the energy increased from 1 to 120 keV.

Figure 6 shows the mean counts for incident energies of 1 – 120 keV across the 3 × 3-pixel neighborhood for energy thresholds LT = 20 and HT = 65 keV for CdTe-,

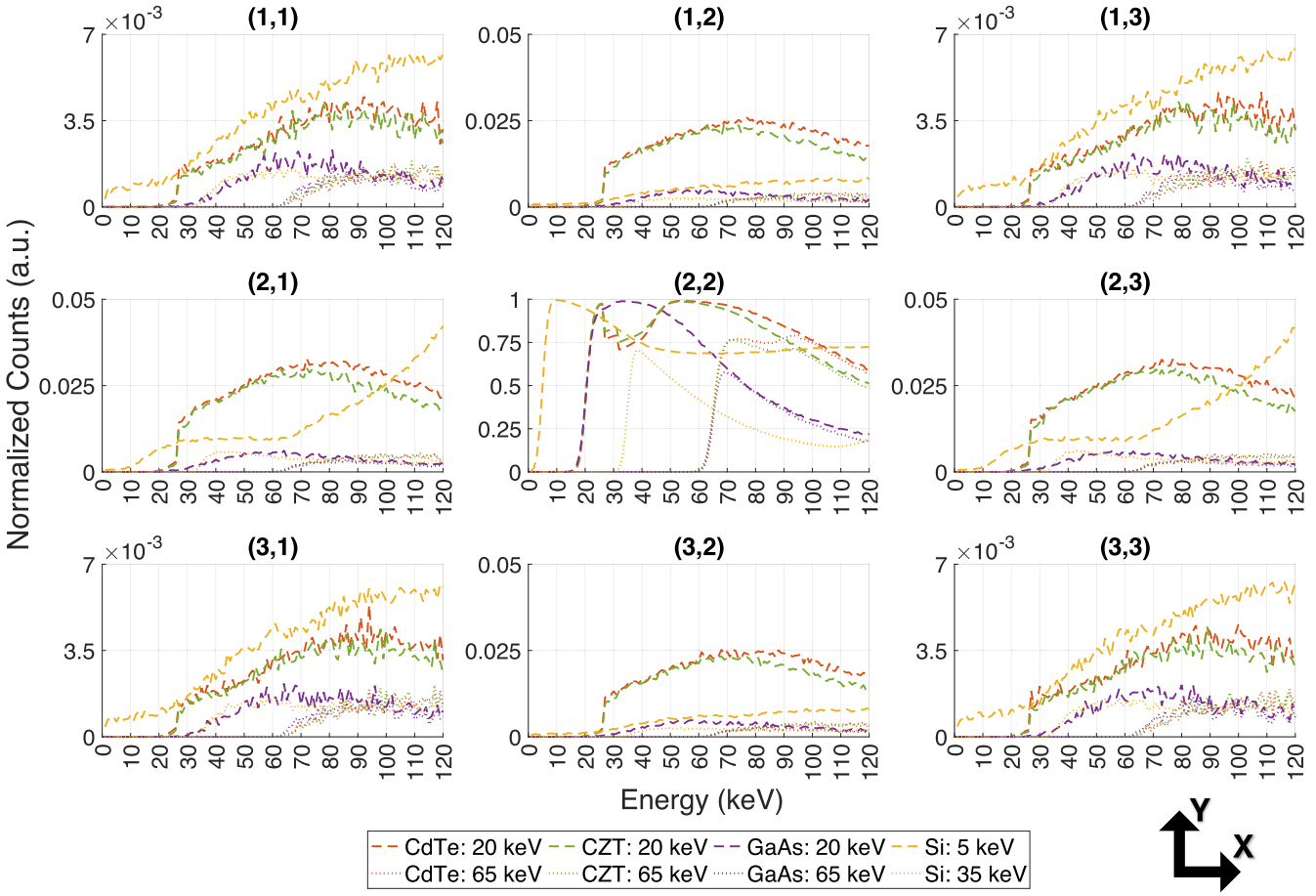

FIGURE 6 Normalized mean counts for incident energies 1–120 keV across 3 × 3-pixel neighborhood. The row and column represent *y*- and *x*-axes, respectively as described in Figure 2. Note that the *y*-axes' values are different.

CZT-, GaAs-PCDs, and LT = 5 keV and HT = 35 keV for Si-PCD designs modeled in this study normalized with the number of incident photons, that is, 1×10^5. The k-edges of Cadmium (Cd) and Tellurium (Te) are visible in CdTe and CZT plots around 27 and 32 keV, respectively. The k-edges of Silicon (Si), Zinc (Zn), Gallium (Ga), and Arsenic (As) are not visible. Si has the lowest magnitude of crosstalk in the neighboring pixels along *y*-axis, specifically in (2, 1) and (2, 3). At the center pixel, CdTe, CZT, and GaAs show a peak in counts that increases to a maximum before decreasing monotonically at higher energies. In contrast, for Si at LT = 5 keV, the counts approach a plateau at higher energies and at HT = 35 keV, the counts decrease monotonically until they plateau again at higher energies.

3.2 | Clinical validation

Figure 7 presents the image quality metrics measured from both real and simulated images across the acquired three dose levels (3.0, 6.0, and 12.0 mGy). The MTF and the nNPS were computed for 20-keV-threshold image while noise magnitude and CT number were computed for all three image types – 20-keV-threshold, 65-keV-threshold, and VMI-70 keV. For the air insert, across all dose levels, the mean absolute differences (MADs) in the f_{90}, f_{50}, and f_{10} were 0.015 $mm^{-1} \pm 0.004$, 0.016 $mm^{-1} \pm 0.004$, and 0.016 $mm^{-1} \pm 0.000$, respectively. Similarly, for the bone insert, these differences were 0.017 $mm^{-1} \pm 0.002$, 0.010 $mm^{-1} \pm 0.006$, and 0.008 $mm^{-1} \pm 0.004$. The f_{av} measured from real and simulated images were 0.271 $mm^{-1} \pm 0.003$ and 0.272 $mm^{-1} \pm 0.000$, respectively.

The relative MADs in noise magnitude measurements for 3.0 mGy dose level were 3.91, 2.42, and 4.28% for 20-keV-threshold, 65-keV-threshold, and VMI-70 keV images. The relative MADs were 0.75%, 1.47%, 0.80% for 6.0 mGy, and 3.30%, 5.26%, 3.24% for 12.0 mGy, respectively. The MADs in CT numbers of the air insert were 0.307 HU ± 0.206, 1.078 HU ± 0.706, 1.086 HU ± 0.389 for 20-keV-threshold, 65-keV-threshold, and VMI-70keV images. For the polyethylene insert, the differences were 2.264 HU ± 0.200, 2.584 HU ± 0.628, and 0.640 HU ± 0.377, respectively.

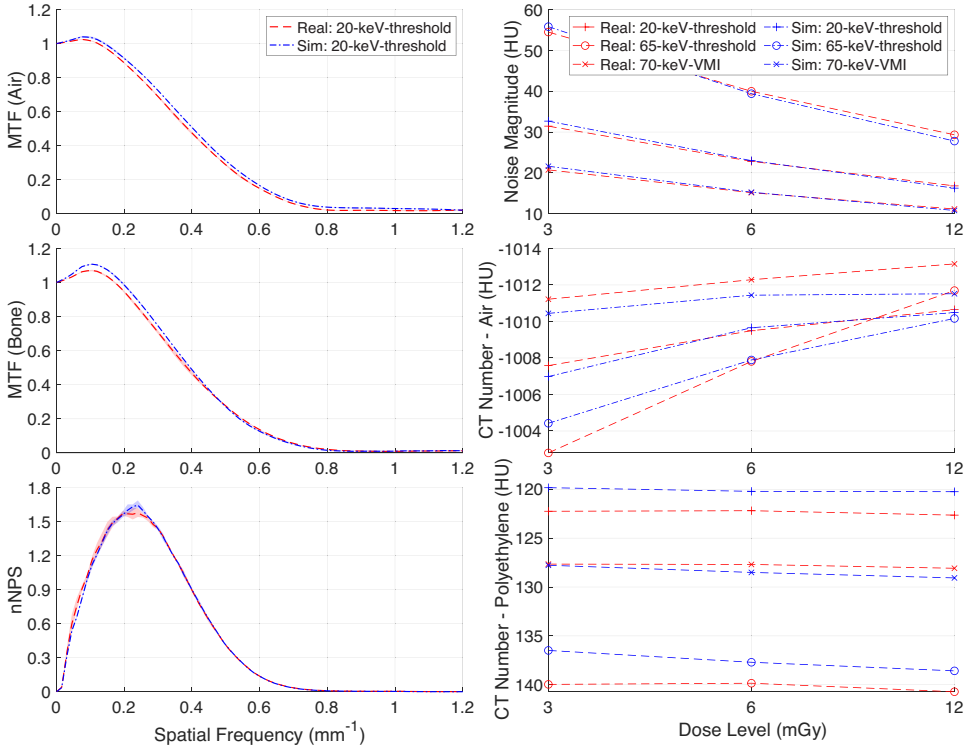

FIGURE 7 Real versus simulated quantitative assessments. MTF, averaged over all dose levels (3.0, 6.0, and 12.0 mGy), for air (top-left) and bone (middle-left) inserts measured from 20-keV threshold images. Normalized NPS, averaged over all dose levels, for 20-keV threshold images (bottom-left). For MTF and nNPS plots, the dotted lines represent the average value while the shaded regions represent the range across all dose levels. Image noise (top-right) measured across all dose levels and image types (20-keV-threshold, 65-keV-threshold, and 70-keV-VMI). CT number of air (middle-right) and polyethylene (bottom-right) inserts measured across all conditions.

TABLE 4 Spatial resolution (f_{50} of MTF), noise magnitude, and CT number for bone insert measured from simulated ACR images across two tube currents and two energy thresholds (Figure 8).

Tube current	Energy threshold	f_{50} (mm^{-1})				Noise Magnitude (HU)				CT Number – Bone (HU)			
		CdTe	CZT	GaAs	Si	CdTe	CZT	GaAs	Si	CdTe	CZT	GaAs	Si
40 mA	LT	0.52	0.52	0.52	0.50	47.6	47.8	55.8	57.4	931.7	945.1	1033.5	927.2
	HT	0.52	0.53	0.51	0.48	73.3	75.2	95.6	78.2	725.2	733.6	756.7	1049.1
200 mA	LT	0.52	0.52	0.52	0.51	21.4	21.6	25.1	26.1	935.4	945.4	1039.3	933.3
	HT	0.53	0.53	0.53	0.51	32.8	33.5	42.5	35.2	726.6	730.6	758.9	1055.4

3.3 | Pilot virtual imaging

Figure 8 shows simulated CT images of the ACR phantom, and Table 4 illustrates the IQ measurements from those images across two energy thresholds (LT, HT) for CdTe-, CZT-, GaAs-, and Si-DukeCounter scanners at 40 and 200 mA. The f_{50} of MTF were within ± 0.05 mm^{-1} range for all DukeCounter scanners across all conditions. The increase in image noise from LT to HT was highest for GaAs at both 40 mA (39.8 HU) and 200 mA (17.4 HU), while lowest for Si at both 40 mA (20.8 HU) and 200 mA (9.1 HU). The difference in CT number measurements for bone insert between LT and HT images at 40 mA were 206.5 HU, 211.5 HU, 276.8 HU, −121.9 HU, and at 200 mA were 208.8 HU, 214.8 HU, 280.4 HU, and −122.1 HU for CdTe-, CZT-, GaAs-, and Si-DukeCounter systems, respectively.

Qualitatively, Figure 9 (left) shows that CT images of the COPD-XCAT phantom appear consistent across all DukeCounter systems. Quantitatively, Table 5 shows that the absolute error in Pi10 measurement and MAE for emphysema vary within ± 0.17 mm and $\pm$ 5.4 HU, respectively, across all DukeCounter scanners. The GaAs-DukeCounter showed the largest deviation in Pi10 from the ground-truth (1.13 mm) and the highest MAE (200.2 HU) for emphysema, while the average

TABLE 5 Quantitative task-specific image quality measurements for COPD quantification and liver lesion detection. Absolute difference in Pi10 measurements and mean absolute error (MAE) in emphysema density between ground-truth and simulated LT images of a COPD-XCAT phantom. CNR and detectability index averaged over six liver lesions obtained from 70 keV mono-energetic CT images of an XCAT with embedded liver lesions.

	DukeCounter scanner	CdTe	CZT	GaAs	Si
COPD XCAT	Absolute difference in Pi10 (mm)	0.94	0.97	1.13	1.08
	Emphysema MAE (HU)	195.8	196.2	200.2	194.8
Liver lesion-XCAT	CNR	1.76 ± 0.16	1.74 ± 0.12	1.43 ± 0.18	1.62 ± 0.28
	Detectability index (d')	4.03 ± 1.07	4.05 ± 1.04	3.10 ± 0.81	3.71 ± 0.99

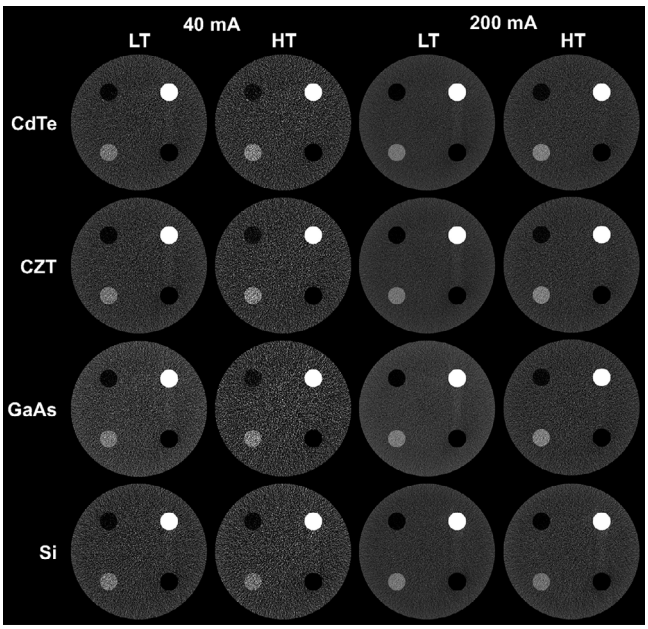

FIGURE 8 Simulated images of an ACR phantom at 40 mA (top row) and 200 mA (bottom row) across LT and HT thresholds for DukeCounter scanners [W/L] = [400/100]. Note that (LT, HT) = (20, 65 keV) for CdTe-, CZT-, GaAs- and (5, 35 keV) for Si-DukeCounter scanners.

deviations were 1.03 mm and 196.8 HU. However, the maximum error observed for GaAs-DukeCounter were not significantly different ($p > 0.05$) than the mean error across all scanners.

Similarly, visually, Figure 9 (right) shows that lesion detectability is consistent across the 70 keV mono-energetic images for all DukeCounter scanners, with the CZT-DukeCounter showing a slight advantage. Table 5 shows that CdTe and GaAs-DukeCounter demonstrated the highest (1.76 ± 0.16) and lowest (1.43 ± 0.18) CNR, while CZT and GaAs-DukeCounter demonstrated the highest (4.05 ± 1.04) and lowest (3.10 ± 0.81) detectability index for liver lesions. CdTe and CZT-DukeCounter had similar performance for liver lesion detectability where the average difference in d' measurements for six lesions was 0.13 ± 0.11.

Task-independent detective quantum efficiency (DQE) for the 0.30 × 0.30 × 1.60 mm^3 CdTe-PCD and 0.50 × 0.50 × 60 mm^3 Si-PCD decreased with increasing water thickness. At their respective Nyquist frequencies, task-independent DQEs for the Si-PCD were 0.239, 0.237, and 0.236 for 20, 30, and 40 cm water thicknesses, respectively, while those for the CdTe-PCD were 0.287, 0.279, and 0.271. These values are consistent with prior studies from which the methodology was adapted, where DQEs of approximately 0.25 for Si and 0.30 for CdTe were estimated visually from the published figures.[12,36,44] Some differences in DQE are likely due to differences in the shape of the source spectrum and the specific energy thresholds used in this study.

4 | DISCUSSION

Photon-counting CT offers high-resolution spectral imaging with promising clinical utilities over conventional energy-integrating CT. For effective clinical adaptation of existing and upcoming technologies, the performance of PCD-CT systems must be evaluated, ideally both task-generically to be applicable to the overall performance across task, but also for targeted task-specific situations. Physical scanners, phantoms, and clinical trials are often costly, time-inefficient, and pose ethical concerns in radiation-based experimentation and lack of ground-truth data.

An efficient approach to overcome these limitations is to utilize a virtual (*in-silico*) imaging framework acquainted with computational PCD-CT scanners and phantom or human models. To generate realistic PCD-CT images, the signal generation process of a photon-counting detector (PCD) must accurately replicate real-world behavior. In our study, this objective was achieved by using Monte Carlo simulation to generate the quantum efficiency of a PCD and blurring it further in both spatial and spectral domains with a charge sharing model. The versatility and viability of this pipeline was demonstrated by simulating CdTe-, CZT-, GaAs-, and Si-based PCD-CT scanners (named DukeCounter scanners) to generate images of an ACR phantom and human models with COPD and liver lesions under varying acquisition conditions.

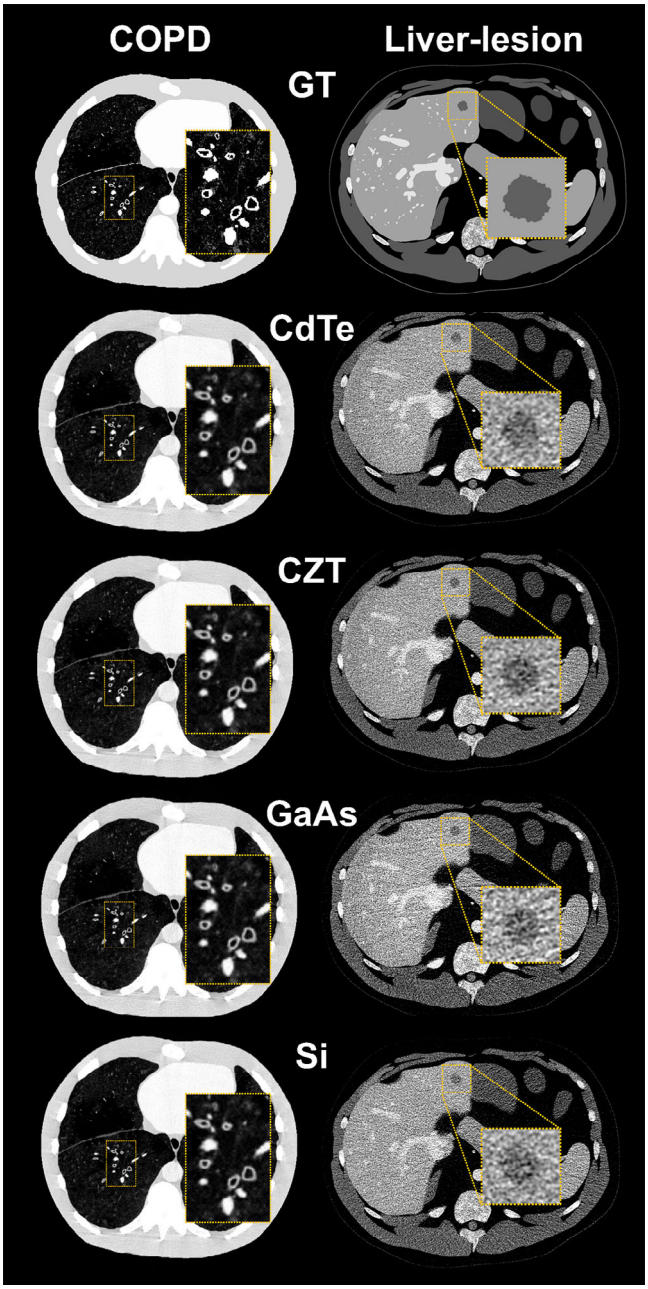

FIGURE 9 Ground-truth (GT) and simulated CT images obtained using DukeCounter scanners. **Left**: COPD-XCAT phantom scanned at 320 mA, displayed with [W/L] = [−450/1000]. COPD CT images are LT images, with zoomed-in views highlighting airway wall thickness. **Right**: XCAT phantom with embedded liver lesions scanned at 240 mA, displayed with [W/L] = [100/300]. Liver lesion CT images are 70-keV mono-energetic images, with zoomed-in views illustrating one of the six lesions.

Several cascaded, analytical, and Monte Carlo-based models have been developed to model the detective quantum efficiencies for PCDs.[5–12] These studies do not offer generalizability across PCD designs or validation against physical measurements. While some validated simulations of clinical and experimental prototype PCD-CT scanners exist, they do not target cross-scanner or cross-detector differences.[14,15] There is a need for a customizable, validated framework applicable across the diversity of PCD-CT technologies. We aimed to create such a framework including diverse detector material properties and dimensions, and their corresponding effect on CT images. This approach enables a direct understanding of the impact of PCD characteristics on resulting CT image quality. Furthermore, our framework efficiently generates clinically relevant PCD-CT images with realistic statistical properties through noise modeling, making it a valuable resource for studies that require large datasets.

This framework was validated against the data from a clinical CdTe-based PCD-CT scanner across various image acquisition settings. The simulated and experimental MTF for air and bone inserts and their corresponding cut-off frequencies (f_{90}, f_{50}, and f_{10}) showed close agreement, confirming the accuracy of the modeled crosstalk processes (Compton and fluorescence scatterings and charge sharing). Slight edge-enhancement observed in the simulated CT images from their MTFs can be attributed to the voxelized nature of the computational phantom, which features sharp boundaries and lacks sub-voxel variations. Additionally, noise texture and noise magnitude were highly consistent between real and simulated ACR images across all image types, validating the accuracy of spatio-energetic mean and covariance matrices. CT numbers for air and polyethylene inserts were consistent across all image types, with particularly close agreement in 70-keV-VMI images. This highlights the accuracy of the simulation for dual energy threshold systems, as VMI images are extracted from the threshold data. Consistency of CT numbers and image noise between real and simulated data across two energy thresholds (20 and 65 keV) as well as 70 keV monoenergetic images provided indirect evidence of spectral consistency. Moreover, our prior work had utilized similar photon transport and charge sharing approach to model an experimental CdTe-based detector (PixiRad-1/Pixie-III, 650 μm thickness, 62 × 62 μm pixel pitch).[13] It showed strong agreement between experimental and simulated spectra for 26, 33, 37, and 50 keV energies under various pixel summing and inhibition modes, providing additional evidence in the accuracy of our spectral response modeling.

While experimental validation was performed using a clinical CdTe-based PCD-CT system, the modeling of CZT-, GaAs-, and Si-based PCDs followed standardized simulation protocols based on well-established, material-specific physical principles.[8,9,45] Validating a physics-based simulation framework across many settings is experimentally unattainable. The limited accessibility of PCDs and vendor-controlled protocol settings made comprehensive validation across all PCD materials, designs, and energy threshold settings infeasible. As such, our study followed the same approach as others to use one PCD material and configuration for

validation.[9,46] The successful validation with a clinical scanner provided confidence in both the physical accuracy and the customizable feature of the framework, as DukeCounter was adapted to replicate a clinical PCD-CT system for validation.

The initial charge cloud size increased with energy for all materials, but more rapidly for Si compared to the others (Figure 5). Our findings are consistent with the Kanaya-Okayama radius, which predicts that the maximum penetration distance of an electron is directly proportional to its energy and inversely proportional to the material's effective Z and density.[10] We computed the initial charge cloud size using MC simulations rather than analytical approximations to be consistent with the MC-based modeling of photon transport and x-ray crosstalk. The normalized counts for CdTe-, CZT-, and GaAs-based PCDs exhibited nearly homogenous distribution around the central pixel, whereas in Si-based PCD, the presence of Tungsten foils along *y*-axis was evident by the lower counts in pixels (2, 1) and (2, 3) as compared to (1, 2) and (3, 2). The drop in counts at the center pixel from lower to higher energies was most distinct for GaAs-PCD, attributable to its low-Z characteristics. Despite of the low Z value of Si, the edge-on design increased the attenuation, and the Tungsten foils minimized the crosstalk in Si-PCD. Secondary peaks corresponding to the k-edges of Cd and Te were visible in the low threshold (= 20 keV) plots of CdTe and CZT. However, the k-edges of Si, Zn, Ga, and As fell below 20 keV and were not observed. Both CdTe and CZT demonstrated similar trends for LT and HT across the 3 × 3-pixel neighborhood with counts increasing to a peak and then decreasing monotonically at higher energies due to the reduced attenuation; however, at the higher energies, CdTe-PCD exhibited slightly higher counts than CZT-PCD due to CZT's comparatively lower attenuation. The rise or plateauing of counts at higher energies for Si, in contrast to other materials, is attributed to the reduced scattering angle at higher energies as predicted by the Klein-Nishina relationship for Compton scattering. This smaller-angle, forward-directed scattering led an increased signal concentration within the 3 × 3-pixel neighborhood and along the z-axis (60 mm thickness). For all PCDs and energy thresholds (LT and HT), electronic noise in the modeling process resulted in non-zero counts below the threshold energies.

For all the modeled DukeCounter scanners, the spatial resolution and noise texture remained consistent across tube currents and energy thresholds, indicating greater sensitivity to reconstruction parameters than to dose level or energy thresholds. Si-DukeCounter exhibited the highest noise magnitude for the low threshold images, despite the low threshold being defined as 5 keV for Si-DukeCounter as compared to 20 keV for others. This is because the counts at the center pixel around the effective energy of the source spectrum are lower for Si-PCD as shown in Figure 6. The HU of bone insert decreased from LT to HT threshold images for the CdTe-, CZT-, and GaAs-DukeCounter, while it increased for the Si-DukeCounter under identical imaging conditions. This behavior can be attributed to the attenuation of bone, which decreases more rapidly than water with increasing energy, and the count magnitudes for PCDs at higher energies (Figure 6). For GaAs-PCD, the contribution of higher energies to the low threshold counts are lowest than for other PCDs. Similarly, for Si-PCD, the contribution of higher energies to the high threshold counts are lowest than for other PCDs. This explains the increase in HU of bone from the low threshold to the high threshold image for Si-DukeCounter, highlighting the dependance of HU variations on the physical properties of the PCDs and energy thresholds. It is important to note that the energy binning (or thresholding) approach can vary among PCDs. For instance, a prototype deep Si-PCD-CT scanner utilized eight energy bins for better spectral separation and detection efficiency.[47] In this study, the two energy thresholds for Si-PCD, 5 keV and 35 keV, resulted in two energy bins – [5 keV to 120 keV] and [35 keV to 120 keV]. These bins are primarily influenced by Compton scatter interactions and photoelectric absorption events, respectively. Qualitatively, CT images of the human models were similar across all DukeCounter scanners as the images for a particular study were acquired and reconstructed under the same settings. Quantitatively, the slight lower task performance for GaAs can be attributed to its image noise and lower signal separability at 70 keV between two thresholds (Figure 6) as the 70 keV mono-energetic images were derived from low- and high-threshold images.

When proprietary details of PCD-CT scanners are not available, the model can be adapted by tuning key parameters such as pixel size, detector thickness, and bias voltage, and validating its output against empirical measurements from the target system. This approach can replicate the system performance across diverse conditions; however, certain proprietary elements may subtly influence spectral or noise characteristics and limit ultimate accuracy. In such cases, sensitivity analyses can be performed to identify the scanner or detector parameters that have the maximum impact on imaging metrics and require tighter constraints, and the ones that have negligible impact and can be approximated more freely. This approach would make the model both customizable and reliable by acknowledging the potential loss of fidelity when complete CT specifications are unavailable.[48]

Pulse pileup was not modeled in this study as its effects have not shown demonstrative impact in clinically-relevant imaging conditions. The 75th percentile of Diagnostic Reference Level for chest-abdomen-pelvis exams for 21–25 cm patients is 10 mGy ($CTDI_{vol}$).[49] Our framework's validation held true at a 12 mGy dose level across low and high energy-threshold and virtual-monoenergetic images. That suggests that

there was no significant impact of pulse pileup in a clinical PCD-CT scanner. Furthermore, one study examined the effects of pileup at very high, maximum achievable exposure levels and found no evidence of pileup, possibly due to small pixel size, short deadtime, or built-in pulse pileup correction mechanisms.[3]

This study had a few limitations. Firstly, while we validated our simulation framework against a clinical CdTe-based PCD-CT scanner, which provides confidence in the approach, such validation was not possible for other detector PCD-CTs due to the lack of experimental data. Secondly, the comparisons that we offer do not relate to any specific PCD-CT technology prototyped or implemented as the specifications of such technologies can vary from those modeled in this work. Furthermore, unique challenges associated with individual PCD technology were not modeled in this work. For instance, charge trapping, and crystal impurities and defects are more pronounced in CZT and GaAs-based PCDs, which can impact their performance.[50,51] Thirdly, based on our validation results across clinically relevant dose levels and a prior study that demonstrated no significant impact of pulse pileup at the maximum achievable exposure level – both conducted on a CdTe-based PCD-CT – we did not integrate a pulse pileup model into our framework.[3] This assumption could extend to PCD-CT systems using other detector materials, such as Si, GaAs, and CZT, which have lower Z_{eff}, higher charge carrier mobility, faster charge collection times, leading to reduced pulse pileup compared to CdTe.[9] Additionally, several pulse pileup correction mechanisms are available, both pre- and post-readout, to mitigate pileup effects.[52–55] However, a comprehensive study evaluating whether pulse pileup remains negligible at clinical dose levels across various PCD-CT systems would strengthen this assumption.

5 | CONCLUSION

We developed and validated a customizable model to simulate the signal generation process across different PCD-CT scanners. CdTe-, CZT-, GaAs-, and Si-based PCDs were designed, and their spatio-energetic detector responses were generated and integrated into a virtual imaging framework along with standardized CT specifications to create DukeCounter PCD-CT scanners. To demonstrate the utility of this framework in characterizing PCD-CT technologies, a computational ACR phantom and anthropomorphic XCAT human models with COPD and liver lesions were scanned with the DukeCounter scanners to measure task-generic image quality metrics, COPD biomarkers, and lesion detectability. This framework provides the flexibility to customize PCD designs and evaluate their impact on both task-generic and task-specific image quality.

ACKNOWLEDGMENTS

The authors would like to thank Karl Stierstorfer (Siemens Healthineers) and Brian Yanoff (GE Healthcare) for valuable discussions. This study was supported by the NIH under grants P41EB028744, R01EB001838, and R01HL155293.

CONFLICT OF INTEREST STATEMENT

Ehsan Samei lists relationships with GE, Siemens, Imalogix, Metis Health Analytics, Silomedics, Cambridge University Press, and Wiley and Sons. Ehsan Abadi lists relationships with GE, Siemens, and Silomedics. William P. Segars lists relationships with Silomedics.

All relationships are unrelated to this publication.

REFERENCES

1. Bhattarai M, Bache S, Abadi E, Samei E. A systematic task-based image quality assessment of photon-counting and energy integrating CT as a function of reconstruction kernel and phantom size. *Med Phys*. 2024;51(2):1047-1060. doi:10.1002/mp.16619
2. Willemink MJ, Persson M, Pourmorteza A, Pelc NJ, Fleischmann D. Photon-counting CT: technical principles and clinical prospects. *Radiology*. 2018;289(2):293-312. doi:10.1148/radiol.2018172656
3. Bhattarai M, Bache S, Abadi E, Samei E. Exploration of the pulse pileup effects in a clinical CdTe-based photon-counting computed tomography. *Med Phys*. 2023;50(11):6693-6703. doi:10.1002/mp.16671
4. Abadi E, Segars WP, Tsui BMW, et al. Virtual clinical trials in medical imaging: a review. *J Med Imaging (Bellingham)*. 2020;7(4):042805. doi:10.1117/1.JMI.7.4.042805
5. Xu J, Zbijewski W, Gang G, et al. Cascaded systems analysis of photon counting detectors. *Med Phys*. 2014;41(10):101907. doi:10.1118/1.4894733
6. Tanguay J, Yun S, Kim HK, Cunningham IA. Detective quantum efficiency of photon-counting x-ray detectors. *Med Phys*. 2015;42(1):491-509. doi:10.1118/1.4903503
7. Taguchi K, Stierstorfer K, Polster C, Lee O, Kappler S. Spatio-energetic cross-talk in photon counting detectors: numerical detector model (PcTK) and workflow for CT image quality assessment. *Med Phys*. 2018;45(5):1985-1998. doi:10.1002/mp.12863
8. Ghammraoui B, Taguchi K, Glick SJ. Inclusion of a GaAs detector model in the photon counting toolkit software for the study of breast imaging systems. *PLoS One*. 2023;18(6):e0270387. doi:10.1371/journal.pone.0270387
9. Persson M, Wang A, Pelc NJ. Detective quantum efficiency of photon-counting CdTe and Si detectors for computed tomography: a simulation study. *J Med Imaging (Bellingham)*. 2020;7(4):043501. doi:10.1117/1.JMI.7.4.043501
10. Lai X, Cai L, Zimmerman K, et al. *CZT modeling for photon counting computer tomography*. vol 10948. SPIE Medical Imaging. SPIE; 2019.
11. Sundberg C, Persson M, Wikner JJ, Danielsson M. 1-mum spatial resolution in silicon photon-counting CT detectors. *J Med Imaging (Bellingham)*. 2021;8(6):063501. doi:10.1117/1.JMI.8.6.063501
12. Stierstorfer K. Modeling the frequency-dependent detective quantum efficiency of photon-counting x-ray detectors. *Med Phys*. 2018;45(1):156-166. doi:10.1002/mp.12667
13. Sharma S, Vrbaski S, Bhattarai M, Abadi E, Longo R, Samei E. A framework to model charge sharing and pulse pileup for virtual imaging trials of photon-counting CT. *Phys Med Biol*. 2024;69(22):225001 doi:10.1088/1361-6560/ad8b0a

14. Abadi E, Harrawood B, Rajagopal JR, et al. Development of a scanner-specific simulation framework for photon-counting computed tomography. *Biomed Phys Eng Express*. 2019;5(5):055008 doi:10.1088/2057-1976/ab37e9
15. Sharma S, Pal D, Abadi E, Segars P, Hsieh J, Samei E. Deep silicon photon-counting CT: a first simulation-based study for assessing perceptual benefits across diverse anatomies. *Eur J Radiol*. 2024;171:111279. doi:10.1016/j.ejrad.2023.111279
16. Abadi E, Harrawood B, Sharma S, Kapadia A, Segars WP, Samei E. DukeSim: a realistic, rapid, and scanner-specific simulation framework in computed tomography. *IEEE Trans Med Imaging*. 2019;38(6):1457-1465. doi:10.1109/TMI.2018.2886530
17. Bhattarai M, Shin DW, Ho FC, et al. Quantitative accuracy of CT protocols for cross-sectional and longitudinal assessment of COPD: a virtual imaging study. *Proc SPIE Int Soc Opt Eng*. 2025;13405. doi:10.1117/12.3046945
18. Panta RK, Yin Z, Gronberg F, et al. Iodine quantification performance with deep silicon-based photon-counting CT: a virtual imaging trial study. *Phys Med*. 2025;135:105003. doi:10.1016/j.ejmp.2025.105003
19. Panta RK, Yin Z, Grönberg F, et al. Liver fat quantification using deep silicon photon-counting CT: an in silico imaging study. *Radiol Adv*. 2025; doi:10.1093/radadv/umaf031
20. Dahal L, Ghojoghnejad M, Vancoillie L, et al. XCAT 3.0: a comprehensive library of personalized digital twins derived from CT scans. *Med Image Anal*. 2025;103:103636. doi:10.1016/j.media.2025.103636
21. Bhattarai M, Panta RK, Clark D, Segars WP, Abadi E, Samei E. A generic model of semiconductor-based photon-counting detectors for spectral CT. *SPIE;* 2024:561-568.
22. Bhattarai M, Sharma S, Vrbaški S, et al. Simulation of the combined effects of charge sharing and pulse pileup in photon-counting CT. *SPIE;* 2022:590-596.
23. Dreier ES, Kehres J, Khalil M, et al. Spectral correction algorithm for multispectral CdTe x-ray detectors. *Opt Eng*. 2018;57(5):054117.
24. Buttacavoli A, Principato F, Gerardi G, et al. Room-temperature performance of 3 mm-thick cadmium-zinc-telluride pixel detectors with sub-millimetre pixelization. *J Synchrotron Radiat*. 2020;27(Pt 5):1180-1189. doi:10.1107/S1600577520008942
25. Sundberg C, Persson M, Sjolin M, Wikner JJ, Danielsson M. Silicon photon-counting detector for full-field CT using an ASIC with adjustable shaping time. *J Med Imaging (Bellingham)*. 2020;7(5):053503. doi:10.1117/1.JMI.7.5.053503
26. Bornefalk H, Danielsson M. Photon-counting spectral computed tomography using silicon strip detectors: a feasibility study. *Phys Med Biol*. 2010;55(7):1999-2022. doi:10.1088/0031-9155/55/7/014
27. Schlomka JP, Roessl E, Dorscheid R, et al. Experimental feasibility of multi-energy photon-counting K-edge imaging in pre-clinical computed tomography. *Phys Med Biol*. 2008;53(15):4031-47. doi:10.1088/0031-9155/53/15/002
28. Yu Z, Leng S, Jorgensen SM, et al. Evaluation of conventional imaging performance in a research whole-body CT system with a photon-counting detector array. *Phys Med Biol*. 2016;61(4):1572-95. doi:10.1088/0031-9155/61/4/1572
29. Xu C, Chen H, Persson M, et al. Energy resolution of a segmented silicon strip detector for photon-counting spectral CT. *Nucl Instrum Meth A*. 2013;715:11-17. doi:10.1016/j.nima.2013.02.030
30. Almqvist H, Crotty D, Nyren S, et al. Initial clinical images from a second-generation prototype silicon-based photon-counting computed tomography system. *Acad Radiol*. 2024;31(2):572-581. doi:10.1016/j.acra.2023.06.031
31. Yang Y, Zhong T, Li H, Lai X. Spectral response of an edge-on gaascr detector for clinical photon counting CT. 2024:1-1.
32. Greiffenberg D, Andra M, Barten R, et al. Characterization of chromium compensated gaas sensors with the charge-integrating JUNGFRAU readout chip by means of a highly collimated pencil beam. *Sensors (Basel)*. 2021;21(4):1550 doi:10.3390/s21041550
33. Bujila R, Omar A, Poludniowski G. A validation of SpekPy: a software toolkit for modelling X-ray tube spectra. *Phys Med*. 2020;75:44-54. doi:10.1016/j.ejmp.2020.04.026
34. Yang K, Ruan C, Li X, Liu B. Data of CT bow tie filter profiles from three modern CT scanners. *Data Brief*. 2019;25:104261. doi:10.1016/j.dib.2019.104261
35. Scarfe WC, Farman AG. What is cone-beam CT and how does it work? *Dent Clin North Am*. 2008;52(4):707-30. doi:10.1016/j.cden.2008.05.005
36. Stierstorfer K, Hupfer M, Koster N. Modeling the DQE(f) of photon-counting detectors: impact of the pixel sensitivity profile. *Phys Med Biol*. 2019;64(10):105008. doi:10.1088/1361-6560/ab1766
37. Abadi E, Jadick G, Lynch DA, Segars WP, Samei E. Emphysema quantifications with CT scan: assessing the effects of acquisition protocols and imaging parameters using virtual imaging trials. *Chest*. 2023;163(5):1084-1100. doi:10.1016/j.chest.2022.11.033
38. Ho FC, Sotoudeh-Paima S, Segars WP, Samei E, Abadi E. Development and application of a virtual imaging trial framework for airway quantifications via CT. *Proc SPIE Int Soc Opt Eng*. Feb 2023;12463 doi:10.1117/12.2654263
39. Bhattarai M, Ho FC, Panta RK, et al. *Edge-on Irradiated Silicon-Based Photon-Counting CT Vs. Energy-Integrating CT for Bronchitis Quantification: A Virtual Imaging Trial Study*. AAPM; 2023:
40. Felice N, Wildman-Tobriner B, Segars WP, et al. Photon-counting computed tomography versus energy-integrating computed tomography for detection of small liver lesions: comparison using a virtual framework imaging. *J Med Imaging (Bellingham)*. 2024;11(5):053502. doi:10.1117/1.JMI.11.5.053502
41. Clark DP, Badea CT. MCR toolkit: a GPU-based toolkit for multi-channel reconstruction of preclinical and clinical x-ray CT data. *Med Phys* 2023;50(8):4775-96. doi:10.1002/mp.16532
42. McCollough CH, Boedeker K, Cody D, et al. Principles and applications of multienergy CT: report of AAPM task group 291. *Med Phys*. 2020;47(7):e881-e912. doi:10.1002/mp.14157
43. Smith TB, Solomon J, Samei E. Estimating detectability index in vivo: development and validation of an automated methodology. *J Med Imaging (Bellingham)*. 2018;5(3):031403. doi:10.1117/1.JMI.5.3.031403
44. Stierstorfer K, Hupfer M. A Monte Carlo method to assess the spectral performance of photon counting detectors. *Med Phys*. 2025;52(3):1515-1525. doi:10.1002/mp.17577
45. Flohr T, Schmidt B. Technical basics and clinical benefits of photon-counting CT. *Invest Radiol*. 2023;58(7):441-450. doi:10.1097/RLI.0000000000000980
46. Taguchi K, Iwanczyk JS. Vision 20/20: single photon counting x-ray detectors in medical imaging. *Med Phys*. 2013;40(10):100901. doi:10.1118/1.4820371
47. Salyapongse AM, Rose SD, Pickhardt PJ, et al. CT number accuracy and association with object size: a phantom study comparing energy-integrating detector CT and deep silicon photon-counting detector CT. *AJR Am J Roentgenol*. 2023;221(4):539-547. doi:10.2214/AJR.23.29463
48. Abadi E, Barufaldi B, Lago M, et al. Toward widespread use of virtual trials in medical imaging innovation and regulatory science. *Med Phys*. 2024;51(12):9394-9404. doi:10.1002/mp.17442
49. Kanal KM, Butler PF, Sengupta D, Bhargavan-Chatfield M, Coombs LP, Morin RLU, S. Diagnostic reference levels and achievable doses for 10 adult CT examinations. *Radiology*. 2017;284(1):120-133. doi:10.1148/radiol.2017161911
50. Bolotnikov AE, Camarda GS, Cui Y, et al. Characterization and evaluation of extended defects in CZT crystals for gamma-ray detectors. *J Cryst Growth*. 2013;379:46-56. doi: 10.1016/j.jcrysgro.2013.01.048

51. Bisogni MG, Cola A, Fantacci ME. Simulated and experimental spectroscopic performance of GaAs X-ray pixel detectors. *Nucl Instrum Methods Phys Res A*. 2001;466(1):188-193. doi: 10.1016/S0168-9002(01)00844-0
52. Touch M, Clark DP, Barber W, Badea CT. A neural network-based method for spectral distortion correction in photon counting x-ray CT. *Phys Med Biol*. 2016;61(16):6132-53. doi:10.1088/0031-9155/61/16/6132
53. Kang Y, Wu R, Li P, et al. Count rate correction for pulse pileup in CdZnTe photon counting detectors. *Mater Sci Semicond Process*. 2024;173:108142. doi: 10.1016/j.mssp.2024.108142
54. Treb K, Radtke J, Culberson WS, Li K. Simultaneous photon counting and charge integrating for pulse pile-up correction in paralyzable photon counting detectors. *Phys Med Biol*. 2023;68(15):155003 doi:10.1088/1361-6560/ace2a9
55. Murata K, Ogawa K. Influence of pulse pile-up effects on material decomposition with photon-counting CT. 2020:1-2.

How to cite this article: Bhattarai M, Panta RK, Segars WP, Abadi E, Samei E. Development of a customizable model for spectral photon-counting detector CT. *Med Phys*. 2025;52:e70195. https://doi.org/10.1002/mp.70195